RELICS: Strong-lensing Analysis of the Massive Clusters MACS J0308.9+2645 and PLCK G171.9−40.7

Ana Acebron[1] , Nathália Cibirka[1] , Adi Zitrin[1] , Dan Coe[2] , Irene Agulli[1], Keren Sharon[3] , Maruša Bradač[4] , Brenda Frye[5], Rachael C. Livermore[6] , Guillaume Mahler[3], Brett Salmon[2] , Keiichi Umetsu[7] , Larry Bradley[2] , Felipe Andrade-Santos[8] , Roberto Avila[2], Daniela Carrasco[6], Catherine Cerny[3], Nicole G. Czakon[7], William A. Dawson[9] , Austin T. Hoag[4] , Kuang-Han Huang[4], Traci L. Johnson[3] , Christine Jones[8], Shotaro Kikuchihara[10], Daniel Lam[11], Lorenzo Lovisari[8], Ramesh Mainali[5] , Pascal A. Oesch[12] , Sara Ogaz[2], Masami Ouchi[10,13] , Matthew Past[3], Rachel Paterno-Mahler[3], Avery Peterson[3], Russell E. Ryan[2], Irene Sendra-Server[14,15], Daniel P. Stark[5], Victoria Strait[4], Sune Toft[16] , Michele Trenti[6,17] , and Benedetta Vulcani[6]

[1] Physics Department, Ben-Gurion University of the Negev, P.O. Box 653, Be'er-Sheva 8410501, Israel; anaacebronmunoz@gmail.com
[2] Space Telescope Science Institute, 3700 San Martin Drive, Baltimore, MD 21218, USA
[3] Department of Astronomy, University of Michigan, 1085 South University Avenue, Ann Arbor, MI 48109, USA
[4] Department of Physics, University of California, Davis, CA 95616, USA
[5] Department of Astronomy, Steward Observatory, University of Arizona, 933 North Cherry Avenue, Rm N204, Tucson, AZ, 85721, USA
[6] School of Physics, University of Melbourne, VIC 3010, Australia
[7] Institute of Astronomy and Astrophysics, Academia Sinica, P.O. Box 23-141, Taipei 10617, Taiwan
[8] Harvard-Smithsonian Center for Astrophysics, 60 Garden Street, Cambridge, MA 02138, USA
[9] Lawrence Livermore National Laboratory, P.O. Box 808 L-210, Livermore, CA, 94551, USA
[10] Institute for Cosmic Ray Research, The University of Tokyo, 5-1-5 Kashiwanoha, Kashiwa, Chiba 277-8582, Japan
[11] Leiden Observatory, Leiden University, NL-2300 RA Leiden, The Netherlands
[12] Geneva Observatory, University of Geneva, Ch. des Maillettes 51, 1290 Versoix, Switzerland
[13] Kavli Institute for the Physics and Mathematics of the Universe (Kavli IPMU, WPI), The University of Tokyo, Chiba 277-8582, Japan
[14] American School of Warsaw, Warszawska 202, 05-520 Bielawa, Poland
[15] Department of Theoretical Physics, University of Basque Country UPV/EHU, E-48080 Bilbao, Spain
[16] Cosmic Dawn Center, Niels Bohr Institute, University of Copenhagen, Juliane Maries Vej 30, Kbenhavn, DK-2100, Denmark
[17] Australian Research Council, Centre of Excellence for All Sky Astrophysics in 3 Dimensions (ASTRO 3D), Melbourne VIC, Australia

Abstract

Strong gravitational lensing by galaxy clusters has become a powerful tool for probing the high-redshift universe, magnifying distant and faint background galaxies. Reliable strong-lensing (SL) models are crucial for determining the intrinsic properties of distant, magnified sources and for constructing their luminosity function. We present here the first SL analysis of MACS J0308.9+2645 and PLCK G171.9−40.7, two massive galaxy clusters imaged with the *Hubble Space Telescope*, in the framework of the Reionization Lensing Cluster Survey (RELICS). We use the light-traces-mass modeling technique to uncover sets of multiply imaged galaxies and constrain the mass distribution of the clusters. Our SL analysis reveals that both clusters have particularly large Einstein radii ($\theta_E > 30''$ for a source redshift of $z_s = 2$), providing fairly large areas with high magnifications, useful for high-redshift galaxy searches (~ 2 arcmin^2 with $\mu > 5$ to ~ 1 arcmin^2 with $\mu > 10$, similar to a typical *Hubble* Frontier Fields cluster). We also find that MACS J0308.9+2645 hosts a promising, apparently bright ($J \sim 23.2$–24.6 AB), multiply imaged high-redshift candidate at $z \sim 6.4$. These images are among the brightest high-redshift candidates found in RELICS. Our mass models, including magnification maps, are made publicly available for the community through the Mikulski Archive for Space Telescopes.

Key words: galaxies: clusters: individual (MACS J0308.9+2645, PLCK G171.9−40.7) – gravitational lensing: strong

1. Introduction

The study of the early universe provides essential insight into the mechanisms of galaxy formation and evolution over cosmic time, as well as the role played by primeval galaxies in the reionization of the universe (Loeb & Furlanetto 2013). Measuring the number counts of high-redshift galaxies allows us to derive their luminosity function (LF) and its evolution with redshift (e.g., Trenti et al. 2010; Oesch et al. 2014; McLeod et al. 2016; Bouwens et al. 2017a; Livermore et al. 2017), which are extensively used to describe the properties of these sources in a statistical way. In particular, by building up the LF in the rest-frame ultraviolet (UV), it is possible to infer the cosmic star formation rate density at early times and assess the role of early galaxies during reionization (Bunker et al. 2004; Bouwens et al. 2010; Ellis et al. 2013; Finkelstein et al. 2015).

This field, however, faces important observational challenges associated with the reliable detection of distant, low-luminosity galaxies. Massive strong gravitational lenses —such as galaxy clusters—act as natural telescopes, allowing us to peer deeper into the universe and infer the properties of background sources that are below the resolution or sensitivity limit of blank fields at the same depth. While blank-field surveys can provide robust constraints on the bright end of the LF (McLure et al. 2013; Bouwens et al. 2014), strong-lensing (SL) clusters can, in a complementary way, constrain the fainter end by magnifying background sources that would otherwise be too faint to be detected (Richard et al. 2008; Zheng et al. 2012; Coe et al. 2013;

Table 1
Properties of the RELICS Clusters Analyzed in This Work

Cluster	R.A. [J2000]	Decl. [J2000]	Redshift	Scale (kpc arcsec^{-1})	Planck SZ mass[a] [$10^{14} M_\odot$]	Planck SZ rank[b]
MACS J0308.9+2645	03:08:59	+26:45:30	0.356	4.994	10.76	12
PLCK G171.9−40.7	03:12:57	+8:22:19	0.270	4.135	10.71	16

Notes.
[a] The mass estimate corresponds to M500 from Planck Collaboration et al. (2015).
[b] The SZ mass ranking in the *Planck* cluster catalog PSZ2.

Zitrin et al. 2014; Atek et al. 2015; Bouwens et al. 2017b; Livermore et al. 2017).

Thanks to their magnification power, SL by galaxy clusters therefore allows us to characterize background sources in unprecedented detail but also entails a reduced source-plane area, so that strong constraints on the faint end of the high-redshift UV LF are difficult to obtain (Atek et al. 2015, 2018; Bouwens et al. 2017a). The net effect of this magnification bias, i.e., the trade-off between the two competing effects of seeing intrinsically fainter objects but in a smaller probed area (i.e., the area benefiting from high magnifications is correspondingly much smaller), depends on the shape of the high-redshift LF, but generally (and assuming typical LFs), we expect to observe more galaxies thanks to lensing, especially at the apparently brighter end (Turner et al. 1984; Broadhurst et al. 1995; Wyithe et al. 2011).

The recent *Hubble Space Telescope* (*HST*) Treasury program RELICS[18] (Reionization Lensing Cluster Survey; PI: D. Coe 2018, in preparation; D. Coe et al. 2018, in preparation; Cerny et al. 2017; Salmon et al. 2017) aims to uncover a substantial sample of high-redshift galaxies by combining *HST* observations with the magnification power from a large sample of massive galaxy clusters, thus minimizing uncertainties due to cosmic variance. In order to reliably determine the intrinsic properties of background sources, construct their LF, and probe their role in reionization, SL models—especially the derived magnification maps—of these foreground lenses are then crucial.

Assuming a mean background density of sources, larger strong lenses, i.e., those with a larger critical area or Einstein radii, should comprise on average more lensed sources and are thus considered particularly useful lenses. In fact, since these massive clusters sit at the high end of the cosmic mass function, they are also useful for constraining cluster physics (Rasia et al. 2013; Ettori et al. 2015), structure evolution, and cosmological models (Blanchard & Bartlett 1998; Planck Collaboration et al. 2014). However, given the shape of the mass function, more massive lenses are scarcer, with only about a dozen clusters known with effective Einstein radii above 30″ (Broadhurst et al. 2005b; Richard et al. 2010; Zitrin et al. 2017).

In this work, we present the first SL analysis of two massive galaxy clusters from the RELICS sample, MACS J0308.9 +2645 and PLCK G171.9−40.7, performed with our light-traces-mass method (LTM; e.g., Zitrin et al. 2015).

This paper is organized as follows. Section 2 presents the data and observations, and Section 3 describes the adopted SL modeling technique as well as our best-fit models. Our findings are presented and discussed in Section 4. Finally, our conclusions are summarized in Section 5. Throughout this work, we adopt the standard ΛCDM flat cosmological model with the Hubble constant $H_0 = 70$ km s^{-1} Mpc^{-1} and $\Omega_M = 0.3$. Magnitudes are quoted in the AB system. Errors are typically 1σ unless otherwise noted.

2. Target, Data, and Observations

The clusters analyzed in the present work are part of the RELICS cluster sample. The RELICS project aims to analyze 41 massive clusters in order to efficiently search for and study magnified high-redshift galaxies. RELICS targeted 21 among the 34 most massive clusters according to their Sunyaev–Zel'dovich (SZ; Sunyaev & Zel'dovich 1972) mass estimates in the *Planck* catalog (Planck Collaboration et al. 2016) that lacked *HST*/IR imaging. In order to maximize exceptional lenses in the RELICS sample, the other half of the sample was selected based on several criteria, such as mass estimations from X-ray (MCXC; Mantz et al. 2010; Piffaretti et al. 2011), weak lensing (Applegate et al. 2014; Sereno & Paraficz 2014; Umetsu et al. 2014; von der Linden et al. 2014; Hoekstra et al. 2015), and SZ—especially from the South Pole Telescope (Bleem et al. 2014) and Atacama Cosmology Telescope (ACT; Hasselfield & ACT Collaboration 2013) data—as well as lensing-strength predictions for some Sloan Digital Sky Survey clusters (SDSS; Wen et al. 2012; Wong et al. 2013). Each cluster in the sample was then observed for a total of three orbits with the Advanced Camera Survey (ACS; F435W, F606W, F814W) and two orbits with the Wide Field Camera 3 (WFC3/IR; F105W, F125W, F140W, F160W) except for cases where *HST*/ACS archival data were already available.

As detailed in Cerny et al. (2017), the RELICS team has delivered reduced *HST* images and photometric source catalogs for the clusters. The photometry is measured with isophotal apertures by SExtractor (Bertin & Arnouts 1996) in dual-image mode, based on the final drizzled 0″06 images, and Bayesian photometric redshifts (hereafter z_{phot}) are then derived using the Bayesian Photometric Redshift program (BPZ; Benítez 2000; Benítez et al. 2004; Coe et al. 2006) from seven *HST* band imaging data (from RELICS observations and *HST* archival data). These data products are available for the community through the Mikulski Archive for Space Telescopes (MAST).[19]

In this paper, we perform an SL analysis of MACS J0308.9 +2645 (MACS0308 hereafter) and PLCKESZ G171.94-40.65 (PLCK G171.9 hereafter). Some relevant details for the clusters are presented in Table 1.

MACS J0308 ($z = 0.35$), displayed in Figure 1, is part of the X-ray luminous Massive Cluster Survey (MACS) cluster sample (Ebeling et al. 2001). MACS0308 had also been previously observed with the ACS for 0.5 orbits in the F606W

[18] https://relics.stsci.edu/

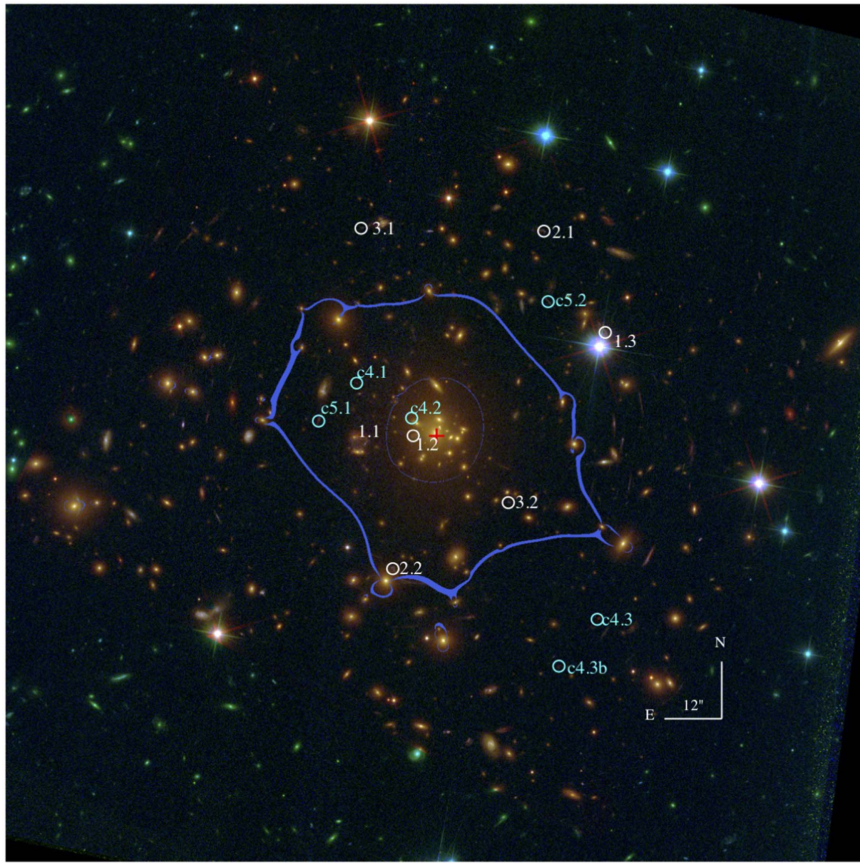[19] https://archive.stsci.edu/prepds/relics/

Figure 1. Color-composite image of MACS0308. Image was created using the *HST*/ACS passbands F435W (blue) and a combination of F606W + F814W (green), and a combination of the *HST*/WFC3IR passbands F105W + F125W + F140W + F160W (red). The critical curves from our best-fit model are displayed in violet for a source at $z \sim 1.15$. The BCG position is indicated with a red cross. Multiple images used as constraints are labeled according to Table 2. Less secure multiple-image candidates are indicated in cyan and are not used as constraints in the modeling.

band and 0.5 orbits in the F814W band (*HST* GO programs 12166, 12884, PI: Ebeling). While the morphology from the X-ray emission map suggests a relaxed and regular cluster, its temperature distribution reveals the presence of two cool cores, possibly associated with an ongoing merger of two substructures (Parekh et al. 2017). A diffuse radio emission was detected as well between these substructures, extending toward the N–S direction.

The other cluster analyzed in this work is PLCK G171.9 ($z = 0.27$), presented in Figure 2. PLCK G171.9 was discovered by *Planck* observations through the SZ effect with a signal-to-noise ratio (S/N) ~ 10.7 and confirmed by *XMM-Newton* X-ray follow-up, which showed that the galactic overdensity was coincident with the X-ray luminosity peak, with the BCG's position only slightly offset from the X-ray peak (Planck Collaboration et al. 2011, 2012). Giacintucci et al. (2013) reported the discovery of a radio halo, often associated with cluster mergers. Indeed, their X-ray analysis of the cluster revealed an asymmetric surface brightness and temperature distribution, which may indicate a disturbed intercluster medium consistent with a recent cluster merger scenario along the NW–SE axis.

3. Lens Modeling

We perform the SL analysis using the LTM method by Zitrin et al. (2009b; see also Broadhurst et al. 2005a; Zitrin et al. 2015). We give here a brief overview of the pipeline. The LTM method is based on the assumption that the general dark matter (DM) distribution in the cluster is traced by the distribution of cluster galaxies, where the mass of each cluster galaxy is generally proportional to its luminosity.

The starting point of the modeling is therefore the identification of cluster members, following the red-sequence method (Gladders & Yee 2000). The magnitudes measured from the F606W and F814W filters are used to draw a color–magnitude diagram, choosing galaxies down to 23 AB within ± 0.3 mag of this sequence, a value often used in the literature (e.g., De Lucia & Poggianti 2008). Stars are excluded from our selection primarily by applying a cutoff value for the stellarity index of <0.95 and only considering objects with magnitudes fainter than 17 AB. We also rely in part on the help of a size–magnitude relation, plotting the FWHM versus the F814W magnitude, to help identify stars which may have been selected. A subsequent visual inspection is performed, discarding further interloping galaxies or artifacts and including high-probability cluster galaxies that were missed in the initial selection. A symmetric power-law surface mass–density distribution, scaling linearly in amplitude with luminosity, is then assigned to each galaxy, defined as

$$\Sigma(r) = K r^{-q}, \tag{1}$$

where r is the galaxy's radius. All galaxies have the same power-law exponent, q, which is a free parameter of the model, and K embeds the linear scaling with the galaxy's measured flux. By integrating Equation (1), the enclosed mass for each
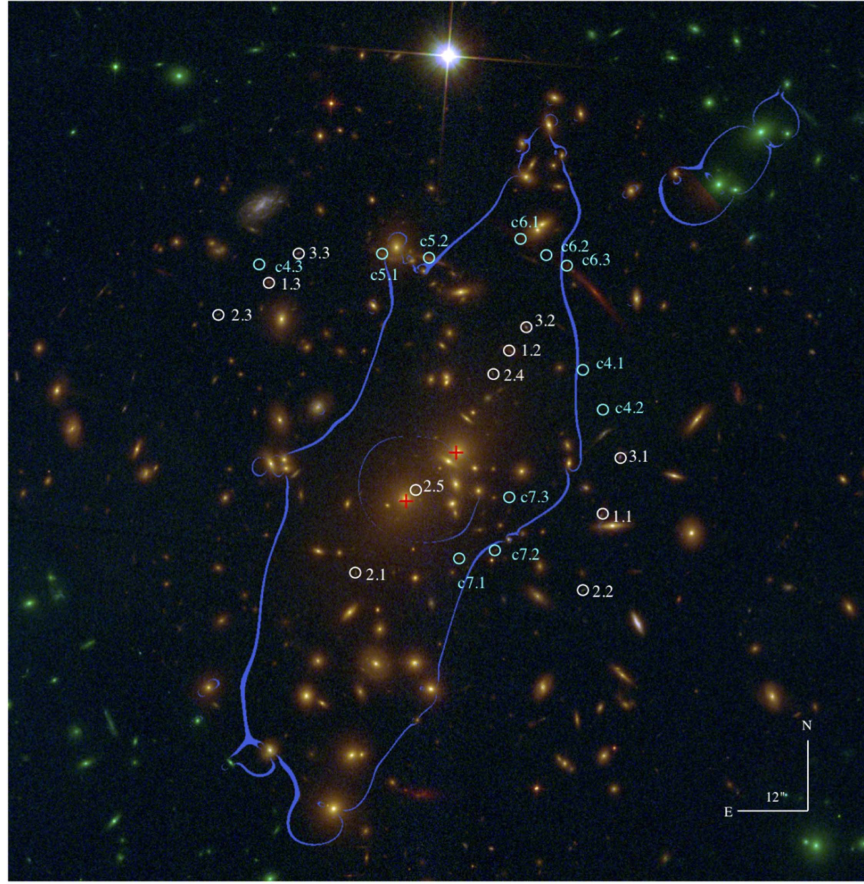
Figure 2. Color-composite image of PLCK G171.9. The image was created using the *HST*/ACS passbands F435W (blue) and a combination of F606W + F814W (green), and a combination of the *HST*/WFC3IR passbands F105W + F125W + F140W + F160W (red). Critical curves from our best-fit model are displayed in violet for a source at $z \sim 2.0$. The two BCG positions are indicated as red crosses. Multiple images used as constraints are labeled according to Table 3. Less secure multiple-image candidates are indicated in cyan and are not used as constraints in the SL modeling.

galaxy is then given by

$$M(<\theta) = \frac{2\pi K}{2 - q}(D_{\rm L}\theta)^{2-q}, \qquad (2)$$

where θ is the angular position and $D_{\rm L}$ is the angular diameter distance to the lens. The sum of all galaxy mass distributions then defines the contribution of the galaxy component of the model.

The deflection angle due to each galaxy is then given by

$$\alpha_{\rm gal}(\theta) = \frac{4GM(<\theta)}{c^2\theta}\frac{D_{\rm LS}}{D_S D_{\rm L}}, \qquad (3)$$

where the galaxy's enclosed mass $M(<\theta) \propto \theta^{2-q}$ is proportional to its luminosity. D_S and $D_{\rm LS}$ are the angular diameter distances to the source and between the lens and the source, respectively. The galaxy's deflection angle can then be rewritten as

$$\alpha_{\rm gal}(\theta) = K_q F \theta^{1-q}, \qquad (4)$$

where K_q is proportional to the lensing distance ratio $D_{\rm LS}/D_S$ and represents the overall normalization.

Since we expect the DM distribution to be smoother, the co-added galaxy distribution is then smoothed with a 2D Gaussian whose width, S, is the second free parameter of the model. From this smooth mass–density map, the deflection field for the DM component of the model, $\alpha_{\rm DM}(\theta)$, is

calculated. The third free parameter is then the scaling of this smooth DM component relative to the total galaxy component, which we denote as $K_{\rm gal}$. The fourth free parameter is the overall normalization, K_q. Since galaxies and the underlying DM distribution are not expected to trace each other rigorously, a two-parameter external shear (introducing a large-scale ellipticity to the magnification map) is also added to allow further flexibility. The external shear is parametrized by its amplitude γ and its position angle ϕ. The total deflection field $\alpha_T(\theta)$ is obtained by adding the contribution of the different components considered in the model,

$$\alpha_T(\theta) = K_{\rm gal}\alpha_{\rm gal}(\theta) + (1 - K_{\rm gal})\alpha_{\rm DM}(\theta) + \alpha_{\rm ex}(\theta), \quad (5)$$

so that the galaxy and the DM components are scaled by the factor $K_{\rm gal}$ and $(1 - K_{\rm gal})$, respectively.

In order to further improve the fit, the relative weight of the brightest cluster galaxies (BCGs) can be freely optimized in the minimization procedure, i.e., they can be allowed to deviate from the *M/L* scaling relation assigned to all other cluster members (see also Von Der Linden et al. 2007; Kormendy & Bender 2013; Newman et al. 2013). In addition, a core and ellipticity can also be introduced for the BCGs, whose parameters—core radius, ellipticity, and position angle, respectively—can also be freely optimized in the minimization procedure, adding more degrees of freedom to the model.

The position and source redshift (where available) of multiple-image families are used as constraints for the SL

Table 2
Multiple Images and Candidates for MACS0308

Arc ID	R.A. [J2000]	Decl. [J2000]	z_{phot} [z_{min}–z_{max}][a]	z_{model} [95% C.I.][b]	Comments	Individual rms (arcsecond)[c]
1.1	03:08:57.171	+26:45:37.22	1.15 [1.12–1.22]	1.15[d]		0.9
1.2	03:08:56.261	+26:45:37.22	⋯	"	In BCG's light	0.8
1.3	03:08:53.345	+26:45:57.32	⋯	"	Behind a star	0.5
2.1	03:08:54.266	+26:46:20.15	1.41 [1.17–2.24]	1.97 [1.80–2.09]		1.1
2.2	03:08:56.611	+26:45:09.16	1.93 [1.83–2.10]	"		0.4
3.1	03:08:57.107	+26:46:20.97	–	1.73 [1.43–1.80]		0.8
3.2	03:08:54.810	+26:45:23.39	1.12 [1.09–2.41]	"		0.9
c4.1	03:08:57.179	+26:45:48.34	6.42 [6.06–6.96]	∼6.4	Not used as constraint	⋯
c4.2	03:08:56.347	+26:45:41.59	⋯	"	Not used as constraint and in BCG's light	⋯
c4.3	03:08:53.407	+26:44:58.93	6.27 [6.14–6.37]	"	"	⋯
c4.3b	03:08:54.027	+26:44:48.71	2.02 [1.67–2.33]	"	"	⋯
c5.1	03:08:57.786	+26:45:40.55	1.12 [1.07–1.37]	∼1.24	Not used as constraint	⋯
c5.2	03:08:54.205	+26:46:05.54	1.22 [0.98–1.71]	"	"	⋯

Notes.
[a] Photometric redshift with upper and lower limits, based on the BPZ estimates from the RELICS catalog with the 95% confidence range. "–" indicates an image for which its z_{phot} could not be measured due to light contamination or poor signal-to-noise ratio.
[b] Redshift prediction based on our best-fit model.
[c] rms between the observed and model-predicted multiple images from our best-fit model.
[d] Fixed redshift.

modeling. The goodness of fit is assessed using a χ^2 criterion quantifying the reproduction of multiple-image positions in the image plane (we assume a positional uncertainty of $0\rlap{.}''5$ for the multiple images), written as

$$\chi^2 = \sum_{i=1}^{n} \frac{(x_i^{pred} - x_i^{obs})^2 + (y_i^{pred} - y_i^{obs})^2}{\sigma_i^2}, \quad (6)$$

with x_i^{obs}, y_i^{obs} and x_i^{pred}, y_i^{pred} being the observed and model-predicted positions of the multiple images, respectively, and σ_i the corresponding positional uncertainty. The optimization of each model is carried out with several thousand Monte Carlo Markov Chain (MCMC) steps. The goodness of fit of a model can also be assessed with the root mean square (rms) between the observed and model-predicted positions of the multiple images in the image plane, which is computed as follows:

$$rms = \sqrt{\frac{1}{N_{img}} \sum_{i=1}^{n} ((x_i^{pred} - x_i^{obs})^2 + (y_i^{pred} - y_i^{obs})^2)}, \quad (7)$$

with N_{img} being the total number of images. Being strongly coupled to the light distribution, so that a minimum of free parameters are needed to generate a mass model while having sufficient flexibility, LTM is a powerful method to both identify new multiple images and constrain the cluster mass distribution (e.g., Zitrin et al. 2015, 2017; see also Broadhurst et al. 2005a). Our SL models typically include about 10–15 total free parameters when accounting, in addition, for freely optimized BCGs and source redshifts where needed.

The LTM method allows to iteratively predict the appearance and orientation of multiple images. Using an initial model constructed by adopting typical parameter values, for example, a typical $q = 1.3$ for the power law or a ∼15% galaxies-to-DM relative weight, we iteratively delens–relens (i.e., send to the source plane and back to the image plane by using the lens equation) multiple-image candidates, in particular distinct-looking or blue arclets, and look in the data for potential, similar-looking counter-images where the initial model predicts them. Multiple-image families are eventually identified—guided by the model's prediction—by their colors, morphology, and symmetry. This process is repeated iteratively as our models are refined using the identified systems. For the modeling, we only use as constraints the position of multiply imaged systems that we consider secure, but also present here other possible multiple-image candidates. While somewhat subjective, by secure systems we refer to those whose agreement with the model prediction, internal details, similar colors, and symmetry leave essentially no doubt that these are images of the same source.

All multiple images presented here are, to our knowledge, the first published for both clusters, and we found no record of spectroscopic redshifts available for any of the systems considered here. Therefore, for each cluster, we fix the redshift of the system with the more reliable photometric estimation to its mean redshift estimate by BPZ, and leave the redshift of other systems as free parameters to be optimized in the minimization procedure (allowing the corresponding D_{LS}/D_S ratio for each system to vary by ±0.2). The implications of such assumptions regarding the accuracy of our SL models (see also Cerny et al. 2017) are further discussed in Section 4.

3.1. MACS J0308.9+2645

In MACS0308, we identified three multiple-image systems, displayed in Figure 1 and listed in Table 2. The first system refers to a spiral galaxy with three multiple images. The third image of this system, 1.3, lies partially behind a star where the LTM predicts it and can be more easily identified in the WFC3/IR images. The second system, comprising two multiple images, has a particular shape that allows for a reliable identification (see Figure 5). The third system is a faint blue galaxy with two multiple images, labeled 3.1 and 3.2. Our model predicts a third, fainter counter-image near the center of

Table 3
Multiple Images and Candidates for PLCK G171.9

Arc ID	R.A. [J2000]	Decl. [J2000]	z_{phot} [z_{min}–z_{max}][a]	z_{model} [95% C.I.][b]	Comments	Individual rms (arcsecond)[c]
1.1	03:12:55.230	+08:22:08.10	2.00 [1.90–2.08]	2.00[d]		1.7
1.2	03:12:56.281	+08:22:36.36	1.98 [1.87–2.10]	"		1.9
1.3	03:12:59.036	+08:22:47.85	1.41 [1.34–2.18]	"		0.4
2.1	03:12:58.043	+08:21:58.16	0.08 [0.07–0.90]	2.10 [2.05–2.58]		3.0
2.2	03:12:55.447	+08:21:55.38	3.34 [0.30–3.50]	"		2.8
2.3	03:12:59.630	+08:22:42.42	3.40 [0.35–3.51]	"		4.1
2.4	03:12:56.467	+08:22:32.21	0.3 [0.10–3.79]	"		0.6
2.5	03:12:57.387	+08:22:12.06	…	"	In BCG's light	1.2
3.1	03:12:55.015	+08:22:18.30	1.99 [1.89–2.16]	2.38 [2.24–2.72]		0.7
3.2	03:12:56.099	+08:22:40.68	2.39 [1.43–2.46]	"		0.9
3.3	03:12:58.699	+08:22:53.04	1.41 [1.40–2.18]	"		1.0
c4.1	03:12:55.503	+08:22:34.21	2.86 [2.15–3.24]	∼3.8	Not used as constraint	…
c4.2	03:12:55.171	+08:22:26.60	…	…	Not used as constraint, sys. can also be high-z	…
c4.3	03:12:59.089	+08:22:50.69	…	…	Not used as constraint, sys. can also be high-z (see text)	…
c5.1	03:12:57.714	+08:22:52.60	…	∼0.86	Not used as constraint	…
c5.2	03:12:57.187	+08:22:51.62	0.84 [0.62-0.90]	…	"	…
c6.1	03:12:55.727	+08:22:51.88	…	∼0.97	Not used as constraint	…
c6.2	03:12:55.970	+08:22:53.43	…	…	"	…
c6.3	03:12:56.254	+08:22:55.95	…	…	"	…
c7.1	3:12:56.871	+8:22:01.05	1.22 [1.15–2.36]	∼1.2	Not used as constraint	…
c7.2	3:12:56.436	+8:22:02.30	2.34 [2.22–2.63]	…	"	…
c7.3	3:12:56.290	+8:22:11.44	0.72 [0.11–0.71]	…	"	…

Notes.
[a] Photometric redshift with upper and lower limits, based on the BPZ estimates from the RELICS catalog with the 95% confidence range. "–" indicates an image for which its z_{phot} could not be measured due to light contamination or poor signal-to-noise ratio.
[b] Redshift prediction based on our best-fit model.
[c] rms between the observed and model-predicted multiple images from our best-fit model.
[d] Fixed redshift.

the cluster but, likely due to its faintness and contamination by the BCG's light, we do not detect it. The reproduction of multiple images identified in this cluster, by our best-fit model, is shown in Figure 5.

Our methodology allows us to predict other sets of multiple images, which we consider less secure and thus do not use them as constraints for our modeling. These candidate systems are designated as such in Table 2 and Figure 1. Candidate system c4 is a drop-out system with $z_{phot} \sim 6.4$ and geometrically predicted to be at high redshift by our model, in agreement with its photometric redshift. This system is among the brightest high-z candidates found in RELICS, and is further discussed in Section 4. The candidate multiple images of system c5 present similar colors, implying that they may be related, and our SL best-fit model predicts $z_{model} \sim 1.24$ for this scenario. In addition to these candidate systems, we note that there are many other elongated, lensed arclets seen in Figure 1, some of which may be in principle multiply imaged, although a lack of internal details and distinct appearance challenge their identification as such. Future dedicated efforts including spectroscopic redshift measurements can help find additional systems in this rich cluster field.

We model MACS0308 leaving as a free parameter the weight of the central BCG. Given its apparent round shape, we assign no ellipticity to the BCG, but allow for a core with

a radius that can reach values of up to 120 kpc. The main source redshift to which we scale our model is set to the photometric redshift of system 1 (with a reliable estimate from BPZ). The redshifts for systems 2 and 3 are left as free parameters of the model and optimized by the SL MCMC modeling pipeline. The critical curves (for a source at $z_s = 1.15$) for our final best-fit model, which has an image reproduction rms = 0″8, are shown in Figure 1.

3.2. PLCK G171.9−40.7

The model for PLCK G171.9 is based on the identification of three multiple-image systems, shown in Figure 2. Their properties are detailed in Table 3. The first and third systems comprise three images each. The second source is multiply imaged into five images. Our model does not predict any further counter-images for these systems.

We find that in our modeling framework, the fit for PLCK G171.9 is improved by allowing the weights of the two central BCGs to vary during the optimization. The ellipticity of the first BCG is left as a free parameter and can vary up to 0.4, whereas the second BCG is also assigned an ellipticity, set to the value measured for it by SExtractor. The core radii of the two BCGs are also left free and can reach values up to 100 kpc. The main source redshift we used for this cluster was set to the photometric redshift of system 1, while the redshift for the

other two systems are again left free to be optimized in the minimization. The final best model has an image reproduction rms = $2\farcs0$, and its resulting critical curves (for a source at $z_s = 2.0$) are shown in Figure 2. The reproduction of multiple images is seen in Figure 6. We also identify other sets of candidate multiple images (considered less secure), listed in Table 3 and displayed in Figure 2. Two images of system c4 form a thin and faint red arc (as seen in the composite ACS/WFC3IR image) straddling the critical curves (images c4.1 and c4.2). Our best-fit SL model predicts a third counter-image at the other side of the cluster, c4.3, and implies a redshift of $z_{model} \sim 3.8$ for this system (however, given the lensing distances involved, it is only possible to determine geometrically from the lensing that the redshift is larger than $\gtrsim 3.5$; in fact, we note that some of the models we probed prefer a higher-redshift solution of $z \sim 6$–7). Given its faintness, a robust z_{phot} estimation for this system is challenging.

The images that we denote c5.1 and c5.2 are similar looking and appear to be lensed, lying next to a few cluster galaxies. However, it is currently unclear whether the two images constitute counter-images of the same source galaxy (with $z_{model} \sim 1.5$), in which case a third counter-image is expected on the other side of the cluster and which we do not clearly identify: one main image and a combination of partial counter-images locally lensed by the adjacent cluster galaxies ($z_{model} \sim 0.86$) or images of two different (but possibly related) galaxies at a somewhat lower redshift. Further detailed examination will be needed to determine the underlying scenario, which we leave for future work.

Candidate system c6 appears as a faint red arc, lying just below a cluster galaxy that evidently contributes to its lensing. The c6 arc might be related to the brighter lensed red arc next to it at R.A. = 03:12:55.30, decl. = +08:22:46.31 (a scenario for which we obtain $z_{model} \sim 0.97$). However, also here the picture is still unclear, and the faint arc, labeled c6.1–c6.2, might only be locally lensed and not at all related to c6.3 (next to the bright arc), a scenario for which our SL model predicts a lower redshift of $z_{model} \sim 0.7$. Finally, we report candidate system c7, composed of two multiple images whose shape and colors are similar and whose parity agrees well with the expected symmetry. Our SL model predicts additional counter-images for this candidate system, one of them we tentatively identify in the data, presented in Table 3, although another close-by image (located at R.A. = 03:12:56.273, decl. = +08:22:14.29) could also be the actual counterpart. Additional images of this system are predicted in the cluster's center and in the northeast region, which we do not detect, possibly due to light contamination and expected faintness.

4. Results and Discussion

The surface mass–density distributions from our best-fit models for MACS0308 and PLCK G171.9, and their azimuthally averaged, radial 1D profiles, are shown in Figure 3. Our modeling of PLCK G171.9 reveals an elongated mass distribution in the NW–SE direction. This finding provides some further evidence for a merger scenario, suggested by previous X-ray studies (Giacintucci et al. 2013). In addition, PLCK G171.9 presents a particularly shallow inner-mass profile, as a result of the two nearby BCGs.

For MACS0308, the mass distribution obtained from our lens modeling shows that it has a slight elongation in the N–S axis, in agreement with that seen in radio observations (Parekh

et al. 2017), implying that the cluster is likely undergoing a merger. We note that the relative 1σ errors on the surface mass–density radial profiles are noticeably smaller than those for PLCK 171.9, in part due to the smaller redshift range spanned by the multiple images behind PLCK 171.9.

Our SL analysis reveals that both MACS0308 and PLCK G171.9 are big lenses, with an effective Einstein radii (defined as $\theta_E = \sqrt{A/\pi}$ with A the critical area, i.e., the area enclosed within the critical curves) of $\theta_E(z_s = 2) = 33 \pm 3''$ and $\theta_E(z_s = 2) = 37 \pm 4''$, respectively. The mass enclosed within the critical curves is $2.5 \pm 0.4 \times 10^{14} M_\odot$ for MACS0308 and $1.3 \pm 0.2 \times 10^{14} M_\odot$ for PLCK G171.9. The uncertainties quoted here correspond to the typical errors found for these quantities, considering both statistical and systematic errors (Zitrin et al. 2015).

Clusters of galaxies with large Einstein radii have proven to be ideal places to search for magnified high-redshift galaxies (e.g., Zheng et al. 2012; Coe et al. 2013; Zitrin et al. 2014; Atek et al. 2015; Kawamata et al. 2016). In Figure 4, we present the magnification maps for a source at $z_s = 9.0$ for both clusters as well as a plot of the resulting cumulative area magnified above each magnification value, i.e., a plot of $A(>\mu)$ versus μ, which can help to assess the strength of the lenses. We find that both clusters cover a fairly large area of high magnification, $\sim 2.85(1.57)$ arcmin^2, for $\mu > 5$ to $\sim 1.56(0.81)$ arcmin^2 for $\mu = 10$, for a source at a redshift of $z_s = 9.0$ for MACS0308 (PLCK G171.9), which might provide in the future interesting objects of the still-elusive high-redshift population (i.e., those that are unreachable with current instruments). In Figure 4 we also mark the corresponding areas $A(\mu > 5)$ and $A(\mu > 10)$ for the *Hubble* Frontier Field clusters (Lotz et al. 2017), computed from the ZITRIN-LTM-GAUSS models (in the respective full area provided). Overall, the lensing strength of both RELICS clusters we analyze here is similar to that of the *Hubble* Frontier Field clusters. Note that while the exact area in which the calculation is made affects the total normalization (the $A(\mu > 0)$ point), its effect diminishes as one goes to higher magnifications, as high magnifications are prominently induced only near the cluster center. Our current choice renders the strength estimation and its comparison to HFF clusters conservative, as our modeling field of view (FOV)—about 6 and 10 arcmin^2 for PLCK G171.9 and MACS0308, respectively—is equal to, or up to two times smaller than, that used for the HFF modeling (between 6 and 20 arcmin^2).

Recently, Salmon et al. (2017) presented the first sample of high-z candidates from RELICS, mainly at $z \sim 6$–8, by performing an independent analysis with two well-known photometric fitting codes, BPZ and Easy and Accurate Z (EZ; Brammer et al. 2008). Lens models, provided following the RELICS observations, can sometimes yield further means to discriminate between photo-z solutions for high-z candidates and allow us to study the source's intrinsic (i.e., demagnified) properties. Regarding the clusters considered in this work, Salmon et al. (2017) have identified six high-z ($z \sim 6$) candidates within MACS0308's FOV and three for PLCK G171.9. Interestingly, MACS0308 hosts the third brightest high-z source from the RELICS sample (Salmon et al. 2017), MACS0308+26-0904 ($J \sim 23.2$ AB), which is substantially sheared.

Our SL model predicts that MACS0308+26-0904 forms a multiply lensed system together with the second brightest high-z source within MACS0308's FOV, designated MACS0308
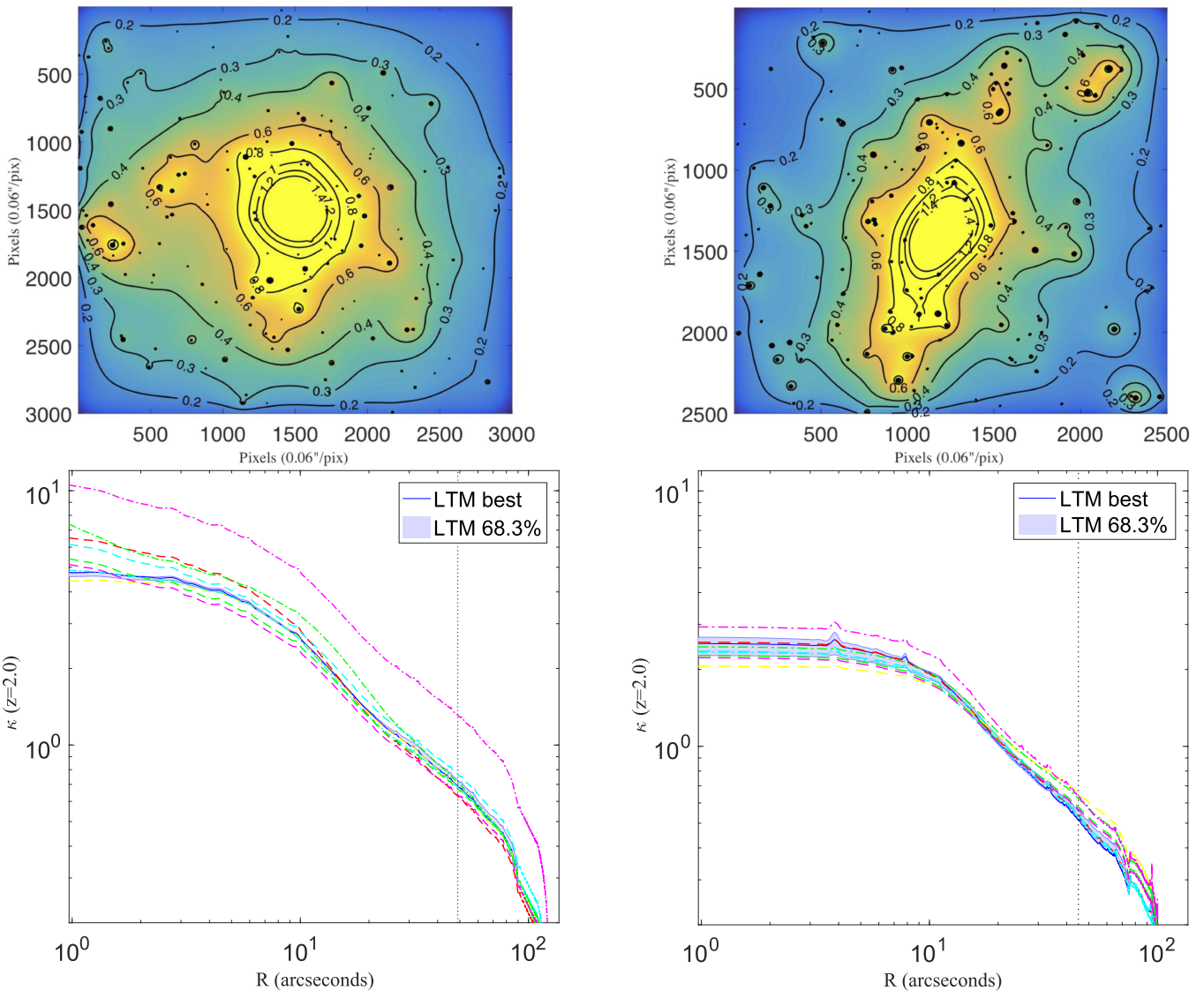
Figure 3. Top panels: map of the convergence, κ, representing the projected surface mass density in units of the critical density for lensing Σ_{crit} and a scaled source redshift of $z_s \sim 2.0$. Bottom panels: the corresponding, azimuthally averaged radial mass–density profile and 1σ errors. The colored dashed lines show the range spanned by the models considering different choices of photometric redshifts. The red and yellow lines are obtained when considering systems 2 and 3 as the main sources with fixed redshifts, respectively. Cyan, green, and magenta dashed and dotted–dashed lines represent models considering a redshift value $\pm10\%$, $\pm25\%$, and $\pm50\%$ (respectively) of that used in the fiducial model (in blue). The black dashed vertical line sets the radius within which we have multiple images. Left column: MACS0308. Right column: PLCK G171.9.

+26-0438 ($J \sim 24.6$ AB). This system is labeled c4 (see Table 2) and our SL model, together with the extensive photometric analysis by Salmon et al. (2017), provide a redshift estimation of $z \sim 6.4$. In addition, being two of the brightest sources in the RELICS high-z candidate sample, these two bright images are thus promising targets for follow-up spectroscopy. The third model-predicted counter-image is predicted near the cluster's center, and thus contaminated by the BCG's light (images c4.1 and c4.2 are radial images, and c4.3 is seen on the other side of the cluster as seen in Figure 1). These images, as well as their reproduction by our SL model, are shown in Figure 5. We also examined another red image of a background source, labeled c4.3b in Table 2, close to our model's predicted location. This source has, however, an estimated photometric redshift $z_{phot} \sim 2.0$ (using BPZ), leading to the conclusion that c4.3 (MACS0308+26-0904) is likely the true counter-image.

We present in Table 4 the high-z candidates detected by Salmon et al. (2017), following their notations, within MACS0308's and PLCK G171.9's FOV. For each high-z candidate, we present a magnification estimate (and statistical uncertainty) from our best-fit model as well as the absolute magnitude, M_{uv}, at $\lambda = 1500\,\text{Å}$. The absolute magnitude is computed from the UV continuum slope $f_\lambda \propto \lambda^\beta$ parametrization for galaxies (Meurer et al. 1999), obtained by a simple weighted least-squares fit using the four WFC3/IR bands (F105W, F125W, F140W, and F160W). The flux corresponding to the redshifted $\lambda = 1500\,\text{Å}$ is then used to obtain the absolute magnitude, given by $M_{AB} = 31.4–2.5\log_{10}(F_{nJy})$. As input we use the BPZ redshift estimate except in ambiguous cases where BPZ predicts a low redshift ($z \sim 1$), for which we then use the EZ estimate (as the scope is to characterize the intrinsic properties of high-z candidates). The resulting rest-frame UV luminosities (corrected for lensing magnifications) have a mean of $M_{uv} \sim -19.45$ and standard deviation of 1.5.
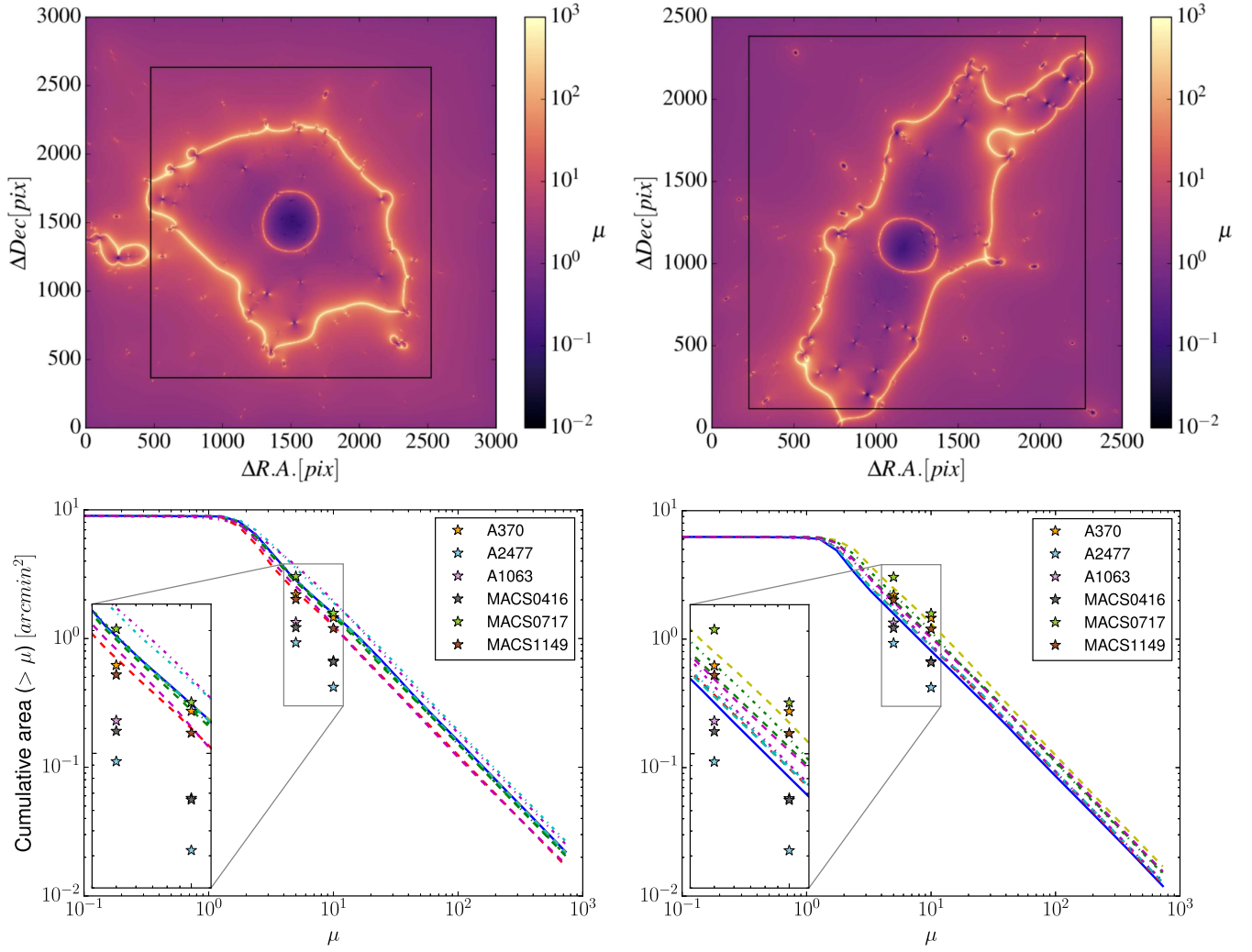
Figure 4. Magnification maps for a source at $z_s = 9.0$ from our best-fit models (upper row). The black rectangle indicates the WFC3/IR FOV. On the bottom row we show the corresponding cumulative area having a magnification higher than a given number for a source at $z_s = 9.0$ (in blue). The colored dashed and dotted–dashed lines show the impact of our uncertainties due to the lack of spectroscopic redshifts with the same color code as in Figure 3. The cumulative areas ($\mu > 5$ and $\mu > 10$) for the *Hubble* Frontier Fields clusters are also indicated as colored stars, computed from the submitted ZITRIN-LTM-GAUSS models. The 1σ errors are typically of the size of the star symbol. Left column: MACS0308. Right column: PLCK G171.9.

Even though recent efforts have aimed at extensively targeting multiple images with ground-based follow-up spectroscopy within the *Hubble* Frontier Fields program for instance (Caminha et al. 2017; Mahler et al. 2018), most other galaxy clusters have, at best, only a few (if any) systems spectroscopically confirmed. Until more data become available, a main limitation of SL modeling lies therefore on the lack of spectroscopic redshifts for the background sources used as constraints (as well as the misidentification of multiple images). In order to accurately determine the mass distribution of the lens, both a reliable estimation of the cosmological distances between the observer and the source and the position of the multiple images on the image plane are crucial. A lens model assuming only photometric redshifts can, for instance, under-predict the mass of the cluster by up to 10% within the Einstein radius (Johnson & Sharon 2016). More recently, Cerny et al. (2017) presented an SL analysis of the first five RELICS clusters and addressed the uncertainties introduced when considering photometrically estimated redshifts. The authors, using a parametric lens-modeling algorithm, found that magnification is still constrained to better than 20% in at least

80% of the FOV even when no spectroscopic redshifts were available.

As neither cluster analyzed here has any multiple image spectroscopically confirmed yet, we have further assessed the robustness of our results (regarding the mass distribution and magnification) by running several models with different combinations of fixed source redshifts or by varying the main source redshift (which was fixed in the fiducial model) by ±10%, ±25%, and ±50%. The resulting azimuthally averaged mass–density profiles and the strength of the lenses, presented as colored dashed lines, are compared to the best-fit model in the bottom panels of Figure 3 and in Figure 4, respectively. We find that, as expected, different combinations of photometric redshifts yield different estimations for the mass profiles, particularly in the inner regions. The mass profiles typically agree within 2σ–3σ, where for the most extreme cases in which we vary the main source redshift, they can differ by ~50%. The Einstein radii inferred from each trial model agree to within 10% and only provide a larger Einstein radius when other redshift combinations are assumed (so that the Einstein radius we quote is on the conservative side). Finally, we have also
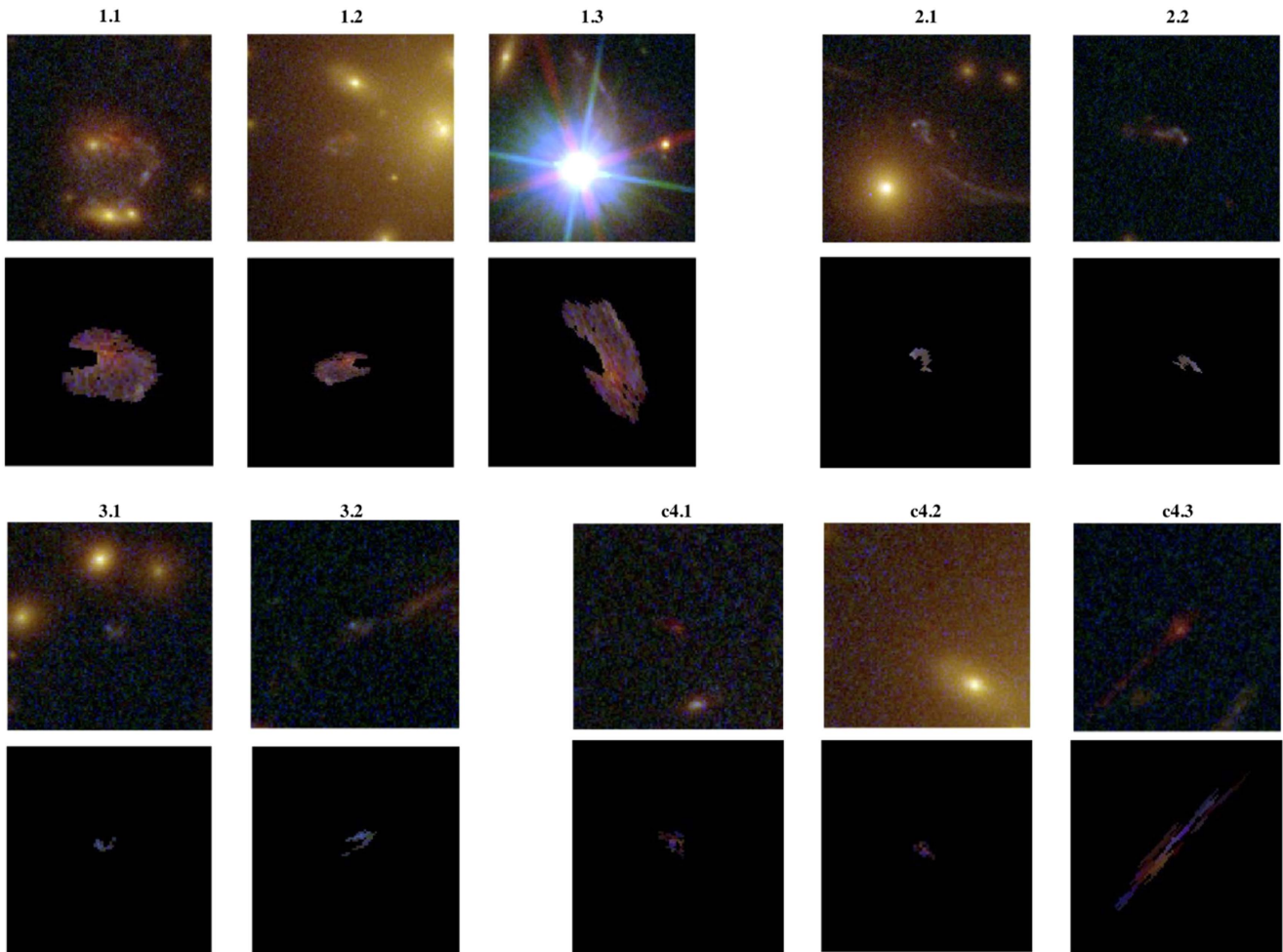
Figure 5. Reproduction of multiple images by our best-fit model for MACS0308. For each image, we delens the first image of the system to the source plane and back to the image plane to compare to the other images of that system. The orientation and internal details of the model-predicted images (bottom rows) are similar to those of the observed images (upper rows).

assessed the impact of redshift uncertainties on the determination of the strength of the lens, in terms of the cumulative magnification seen in Figure 4. While these uncertainties do not have a significant impact for the total magnified area, i.e., the area with magnifications above μ' where μ' is small ($\mu' \lesssim 1$–2), higher magnification regions can suffer up to a 60% bias and, in the case of PLCK G171.9, only increasing the strength of the lens when considering other redshift combinations (so also our magnification estimate appears to be conservative). Overall, we find that magnification at $z = 9$ is constrained to better than 20% in at least 70% and 50% of the modeled FOV when overestimating or underestimating the fixed main source redshift by 10%–25%, respectively, similar to the findings Cerny et al. (2017) obtained with a fully parametric modeling technique. By changing the value of the fixed main source redshift by 50%, the magnification is constrained to better than 30% in around 60% of the modeled FOV. These typical errors include the uncertainties from redshift or cosmological distances and thus, in part, the mass–sheet degeneracy (Falco et al. 1985; Liesenborgs & De Rijcke 2012).

Other sources of systematic errors, which are beyond the scope of this study, should also be taken into account as they can introduce a supplementary bias on magnification such as the presence of noncorrelated line-of-sight halos (D'Aloisio

et al. 2014; Chirivì et al. 2017; Williams et al. 2017), the assumption that light traces mass (Harvey et al. 2016), different modeling choices (Limousin et al. 2016), the triaxial shape of clusters (Giocoli et al. 2014; Sereno et al. 2015), or uncertainties regarding the cosmological parameters (Bayliss et al. 2015). For a more general discussion of systematics in SL analysis, see Zitrin et al. (2015), Meneghetti et al. (2017), and Priewe et al. (2017).

Our SL models are made publicly available through the MAST archive as RELICS high-level science products. We supply deflection fields, surface mass density (κ) maps, and magnification maps for different redshifts, including also a subset of a hundred random models from the MC so that errors can be calculated. An online magnification calculator will also be available (see footnote 2) for fast magnification estimates.

We note that one should be generally cautious when using SL modeling outputs (such as convergence, magnification, etc.) beyond the SL regime where multiple images are seen (roughly twice the Einstein radius), so that the lens models should be considered extrapolations beyond this limit. In addition, in our case, the smoothing and other interpolations used in our methodology often introduce some boundary artifacts, mainly near the edges of the modeled FOV, of which the user should be aware.
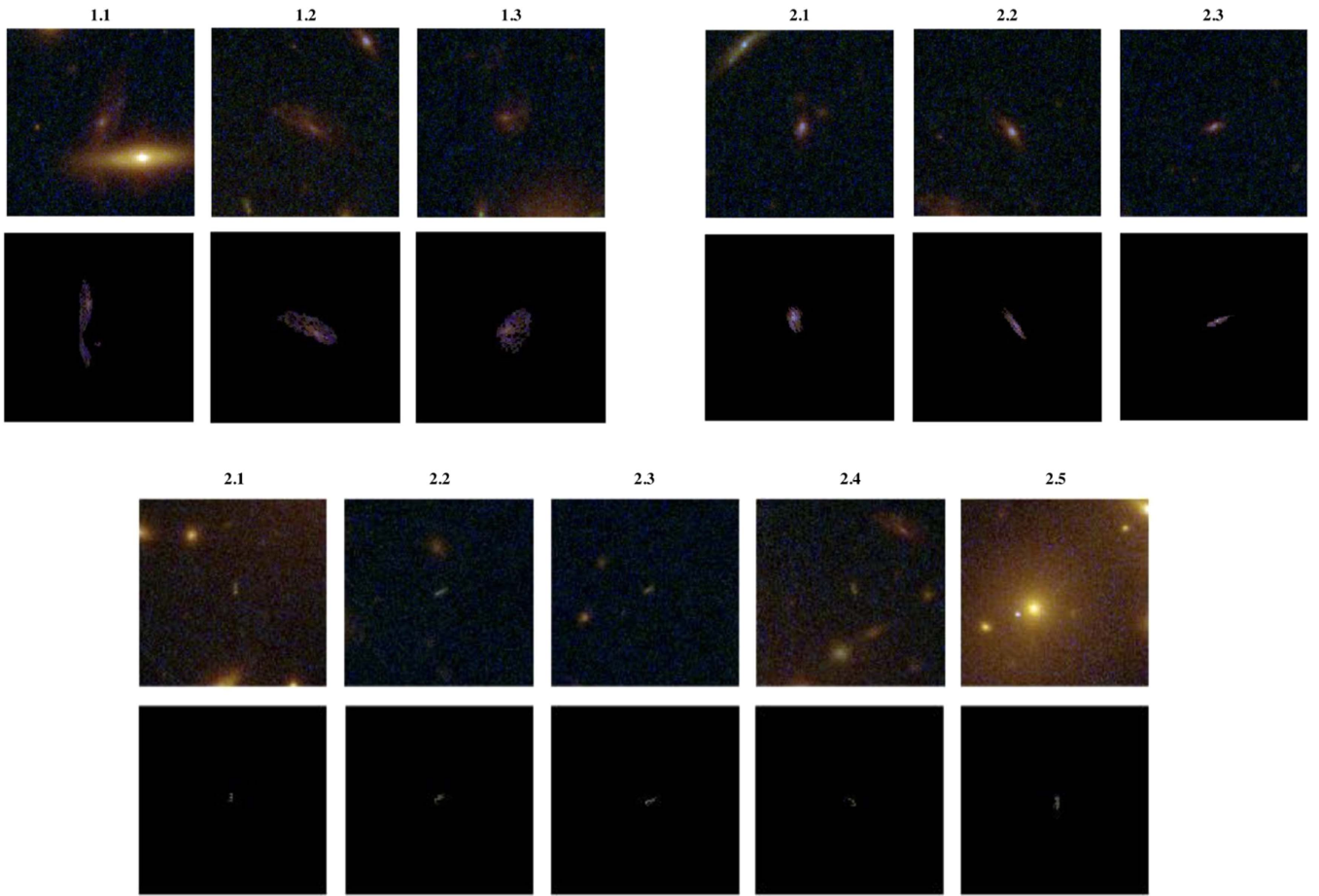
Figure 6. Reproduction of multiple images by our best-fit model for PLCK G171.9. Produced similarly to Figure 5.

5. Summary

In this work, we have analyzed two massive, nonrelaxed clusters from the RELICS cluster sample, MACS J0308.9 +2645 and PLCK G171.9−40.7, that are X-ray and SZ selected, respectively. We presented the first SL analysis of both clusters, adopting a light-traces-mass methodology and uncovering several multiply imaged galaxies in each. Our analysis has revealed that both MACS0308 and PLCK G171.9 are prominent lenses with large Einstein radii, hosting some promising $z \sim 6$ candidates (Salmon et al. 2017). Both clusters are therefore viable targets for spectroscopic follow-up, both to obtain spectroscopic redshifts of the multiple-image systems presented in this work to refine the lens model as well as for studying high-z candidates. In particular, MACS0308 hosts a particularly bright $(J \sim 23.2-24.6\,\mathrm{AB})$ multiply imaged high-z candidate useful for spectroscopic follow-up, with both photometric analysis (Salmon et al. 2017) and our lens model agreeing on its high-redshift nature at $z \sim 6.4$. This source is among the brightest high-z candidates found in all of RELICS.

Our lens models, as well as magnification maps, are made publicly available through the MAST archive (see footnote 2). Massive galaxy clusters with large Einstein radii are also statistically interesting, enabling the high-mass end of the halo distribution to be determined and the theoretical ΛCDM predictions for structure formation and evolution to be probed (Oguri & Blandford 2009; Redlich et al. 2014). In that sense, it should also be noted that the selection function plays a crucial role

and should be taken into account in such comparisons. Moreover, such studies suffer from a modest sample size, as only several to a dozen galaxy clusters with $\theta_E > 30''$ are known to date (see, for instance, Broadhurst et al. 2005a; Limousin et al. 2007; Zitrin et al. 2009a, 2017; Richard et al. 2010; Postman et al. 2012; Cerny et al. 2017). In this work, we present and add to the list two new massive clusters with such large Einstein radii. These will be potentially complemented with other large lensing clusters from the RELICS sample that are now being analyzed.

To estimate leading uncertainties in our models, we explored possible biases due to the lack of spectroscopic redshifts for the multiply imaged systems. We find that, while a refinement of the models is warranted when spectroscopic data become available, our SL models yield a robust measurement (within 10%) of the Einstein radius for both clusters, taking into account both the statistical and systematic errors arising from the lack of spectroscopic data. This translates into a similar value, $\sim15\%$, for the enclosed Einstein mass. For the mass distribution, and in particular the 1D radial mass–density profile, we find that different redshift combinations agree to within 2σ or 3σ. Magnification estimates appear to be more susceptible to the redshift combinations and can reach a 60% discrepancy in areas with high magnification. These values should thus be used more cautiously, taking into account the relevant systematic uncertainties. Additional explicit biases in the quantities derived in this work can be further assessed by comparing our results to those from other independent lens-modeling techniques (Bouwens et al. 2017a; Meneghetti et al. 2017).

Table 4
High-z ($z \sim 6$) Lensed Candidates

Galaxy ID[a]	R.A. [J2000]	Decl. [J2000]	J_{125}[b] [AB]	z_{phot}^{BPZ}[c]	z_{phot}^{EZ}[d]	μ[e]	$M_{uv,1500}$[f] [AB]
MACS0308+26-0904*	03:08:53.407	+26:44:58.93	23.20 ± 0.05	$6.3^{+0.1}_{-0.1}$	$6.4^{+0.2}_{-0.2}$	$16.99(19.11)^{+3.75}_{-2.12}$	$-20.43^{+0.48}_{-0.33}$
MACS0308+26-0438*	03:08:57.189	+26:45:48.37	24.64 ± 0.09	$6.3^{+0.5}_{-0.3}$	$6.4^{+0.5}_{-0.3}$	$2.14(2.24)^{+0.07}_{-0.08}$	$-21.22^{+0.32}_{-0.31}$
MACS0308+26-0249	03:08:57.025	+26:46:07.15	23.75 ± 0.11	$5.6^{+0.2}_{-0.5}$	$1.0^{+0.3}_{-0.1}$	$3.07(3.00)^{+0.09}_{-0.09}$	$-20.66^{+0.31}_{-0.31}$
MACS0308+26-0991	03:08:57.197	+26:44:41.96	25.93 ± 0.22	$5.4^{+0.4}_{-4.8}$	$6.0^{+0.3}_{-1.3}$	$11.93(10.66)^{+1.24}_{-0.94}$	$-17.80^{+0.37}_{-0.87}$
MACS0308+26-0184	03:08:57.288	+26:46:19.27	26.66 ± 0.29	$5.3^{+0.4}_{-1.0}$	$5.7^{+0.4}_{-0.9}$	$3.14(3.17)^{+0.11}_{-0.08}$	$-18.87^{+0.31}_{-0.35}$
MACS0308+26-0575	03:08:51.383	+26:45:36.89	26.93 ± 0.36	$0.9^{+5.1}_{-0.4}$	$5.8^{+0.5}_{-5.1}$	$10.58(13.27)^{+3.55}_{-2.69}$	$-17.12^{+0.71}_{-0.91}$
PLCK G171−40-0130	03:12:54.204	+08:23:03.88	23.93 ± 0.12	$5.7^{+0.3}_{-5.1}$	$5.8^{+0.4}_{-1.1}$	$4.54(6.05)^{+1.30}_{-0.99}$	$-20.77^{+0.63}_{-0.91}$
PLCK G171−40-0355	03:12:57.268	+08:22:35.47	25.41 ± 0.19	$1.0^{+5.0}_{-0.3}$	$5.9^{+0.4}_{-0.8}$	$1.96(2.32)^{+0.14}_{-0.16}$	$-20.53^{+0.35}_{-0.34}$
PLCK G171−40-0738	03:12:57.520	+08:21:51.10	25.35 ± 0.15	$5.5^{+0.3}_{-4.8}$	$5.7^{+0.4}_{-4.7}$	$21.32(32.42)^{+9.93}_{-12.01}$	$-17.62^{+1.16}_{-1.05}$

Notes.
[a] Galaxy ID, following Salmon et al. (2017) notations. The first two high-z candidates, indicated with an asterisk, correspond to the multiply imaged candidates c4.3 and c4.1 in Table 2, respectively.
[b] Apparent magnitude in the F125W band.
[c] Redshift estimation based on the BPZ pipeline along with their 1σ uncertainties.
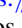[d] Redshift estimation based on the EZ pipeline along with their 1σ uncertainties.
[e] Magnification estimates (at the respective source redshift) from our best-fit model, the average (computed from 100 random MCMC models, in parentheses) and statistical uncertainty. The best-fit value is the one used for all relevant computations.
[f] Absolute magnitude, M_{uv}, at $\lambda = 1500$ Å for which the errors have been propagated from the photometric and magnification uncertainties.
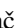
Together with the spectacular imaging data provided by the RELICS project, SL models of the whole cluster sample (see also Cerny et al. 2017; Cibirka et al. 2018) will help divulge exciting high-redshift candidates (Salmon et al. 2018) in time for *James Webb Space Telescope* spectroscopic follow-up.

ORCID iDs

Ana Acebron ⬤ https://orcid.org/0000-0003-3108-9039
Nathália Cibirka ⬤ https://orcid.org/0000-0002-2356-4680
Adi Zitrin ⬤ https://orcid.org/0000-0002-0350-4488
Dan Coe ⬤ https://orcid.org/0000-0001-7410-7669
Keren Sharon ⬤ https://orcid.org/0000-0002-7559-0864
Maruša Bradač ⬤ https://orcid.org/0000-0001-5984-0395
Rachael C. Livermore ⬤ https://orcid.org/0000-0003-4456-1566
Brett Salmon ⬤ https://orcid.org/0000-0002-7453-7279
Keiichi Umetsu ⬤ https://orcid.org/0000-0002-7196-4822
Larry Bradley ⬤ https://orcid.org/0000-0002-7908-9284
Felipe Andrade-Santos ⬤ https://orcid.org/0000-0002-8144-9285
Daniela Carrasco ⬤ https://orcid.org/0000-0002-3772-0330
William A. Dawson ⬤ https://orcid.org/0000-0003-0248-6123
Austin T. Hoag ⬤ https://orcid.org/0000-0001-8989-2567

Kuang-Han Huang ⬤ https://orcid.org/0000-0001-7826-6448
Traci L. Johnson ⬤ https://orcid.org/0000-0002-8829-5303
Ramesh Mainali ⬤ https://orcid.org/0000-0003-0094-6827
Pascal A. Oesch ⬤ https://orcid.org/0000-0001-5851-6649
Masami Ouchi ⬤ https://orcid.org/0000-0002-1049-6658
Sune Toft ⬤ https://orcid.org/0000-0003-3631-7176
Michele Trenti ⬤ https://orcid.org/0000-0001-9391-305X
Benedetta Vulcani ⬤ https://orcid.org/0000-0003-0980-1499

References

Applegate, D. E., von der Linden, A., Kelly, P. L., et al. 2014, MNRAS, 439, 48
Atek, H., Richard, J., Jauzac, M., et al. 2015, ApJ, 814, 69
Atek, H., Richard, J., Kneib, J.-P., & Schaerer, D. 2018, arXiv:1803.09747
Bayliss, M. B., Sharon, K., & Johnson, T. 2015, ApJL, 802, L9
Benítez, N. 2000, ApJ, 536, 571
Benítez, N., Ford, H., Bouwens, R., et al. 2004, ApJS, 150, 1
Bertin, E., & Arnouts, S. 1996, A&As, 117, 393
Blanchard, A., & Bartlett, J. G. 1998, A&A, 332, L49
Bleem, L., Brodwin, M., Ashby, M., et al. 2014, Spitzer Imaging of Massive zgt1 SZ-Selected Galaxy Clusters, Spitzer Proposal
Bouwens, R. J., Illingworth, G. D., Oesch, P. A., et al. 2010, ApJL, 709, L133
Bouwens, R. J., Illingworth, G. D., Oesch, P. A., et al. 2014, ApJ, 793, 115
Bouwens, R. J., Oesch, P. A., Illingworth, G. D., Ellis, R. S., & Stefanon, M. 2017a, ApJ, 843, 129
Bouwens, R. J., van Dokkum, P. G., Illingworth, G. D., et al. 2017b, arXiv:1711.02090
Brammer, G. B., van Dokkum, P. G., & Coppi, P. 2008, ApJ, 686, 1503
Broadhurst, T., Benítez, N., Coe, D., et al. 2005b, ApJ, 621, 53
Broadhurst, T., Takada, M., Umetsu, K., et al. 2005a, ApJL, 619, L143
Broadhurst, T. J., Taylor, A. N., & Peacock, J. A. 1995, ApJ, 438, 49
Bunker, A. J., Stanway, E. R., Ellis, R. S., & McMahon, R. G. 2004, MNRAS, 355, 374
Caminha, G. B., Grillo, C., Rosati, P., et al. 2017, A&A, 607, A93
Cerny, C., Sharon, K., Andrade-Santos, F., et al. 2017, arXiv:1710.09329
Chirivì, G., Suyu, S. H., Grillo, C., et al. 2017, arXiv:1706.07815
Cibirka, N., Acebron, A., Zitrin, A., et al. 2018, arXiv:1803.09557
Coe, D., Benítez, N., Sánchez, S. F., et al. 2006, AJ, 132, 926
Coe, D., Zitrin, A., Carrasco, M., et al. 2013, ApJ, 762, 32
D'Aloisio, A., Natarajan, P., & Shapiro, P. R. 2014, MNRAS, 445, 3581
De Lucia, G., & Poggianti, B. M. 2008, in ASP Conf. Ser. 399, Panoramic Views of Galaxy Formation and Evolution, ed. T. Kodama, T. Yamada, & K. Aoki (San Francisco, CA: ASP), 314

Ebeling, H., Edge, A. C., & Henry, J. P. 2001, ApJ, 553, 668
Ellis, R. S., McLure, R. J., Dunlop, J. S., et al. 2013, ApJL, 763, L7
Ettori, S., Baldi, A., Balestra, I., et al. 2015, A&A, 578, A46
Falco, E. E., Gorenstein, M. V., & Shapiro, I. I. 1985, ApJL, 289, L1
Finkelstein, S. L., Ryan, R. E., Jr., Papovich, C., et al. 2015, ApJ, 810, 71
Giacintucci, S., Kale, R., Wik, D. R., Venturi, T., & Markevitch, M. 2013, ApJ,
    766, 18
Giocoli, C., Meneghetti, M., Metcalf, R. B., Ettori, S., & Moscardini, L. 2014,
    MNRAS, 440, 1899
Gladders, M. D., & Yee, H. K. C. 2000, AJ, 120, 2148
Harvey, D., Kneib, J. P., & Jauzac, M. 2016, MNRAS, 458, 660
Hasselfield, M. & ACT Collaboration 2013, in American Astronomical Society
    Meeting 221, Abstract, 124.05
Hoekstra, H., Herbonnet, R., Muzzin, A., et al. 2015, MNRAS, 449, 685
Johnson, T. L., & Sharon, K. 2016, ApJ, 832, 82
Kawamata, R., Oguri, M., Ishigaki, M., Shimasaku, K., & Ouchi, M. 2016,
    ApJ, 819, 114
Kormendy, J., & Bender, R. 2013, ApJL, 769, L5
Liesenborgs, J., & De Rijcke, S. 2012, MNRAS, 425, 1772
Limousin, M., Richard, J., Jullo, E., et al. 2007, ApJ, 668, 643
Limousin, M., Richard, J., Jullo, E., et al. 2016, A&A, 588, A99
Livermore, R. C., Finkelstein, S. L., & Lotz, J. M. 2017, ApJ, 835, 113
Loeb, A., & Furlanetto, S. R. 2013, The First Galaxies in the Universe
    (Princeton, NJ: Princeton Univ. Press)
Lotz, J. M., Koekemoer, A., Coe, D., et al. 2017, ApJ, 837, 97
Mahler, G., Richard, J., Clément, B., et al. 2018, MNRAS, 473, 663
Mantz, A., Allen, S. W., Ebeling, H., Rapetti, D., & Drlica-Wagner, A. 2010,
    MNRAS, 406, 1773
McLeod, D. J., McLure, R. J., & Dunlop, J. S. 2016, MNRAS, 459, 3812
McLure, R. J., Dunlop, J. S., Bowler, R. A. A., et al. 2013, MNRAS, 432, 2696
Meneghetti, M., Natarajan, P., Coe, D., et al. 2017, MNRAS, 472, 3177
Meurer, G. R., Heckman, T. M., & Calzetti, D. 1999, ApJ, 521, 64
Newman, A. B., Treu, T., Ellis, R. S., et al. 2013, ApJ, 765, 24
Oesch, P. A., Bouwens, R. J., Illingworth, G. D., et al. 2014, ApJ, 786, 108
Oguri, M., & Blandford, R. D. 2009, MNRAS, 392, 930
Parekh, V., Dwarakanath, K. S., Kale, R., & Intema, H. 2017, MNRAS,
    464, 2752

Piffaretti, R., Arnaud, M., Pratt, G. W., Pointecouteau, E., & Melin, J.-B. 2011,
    A&A, 534, A109
Planck Collaboration, Ade, P. A. R., Aghanim, N., et al. 2014, A&A, 571, A20
Planck Collaboration, Ade, P. A. R., Aghanim, N., et al. 2015, A&A, 582, A29
Planck Collaboration, Ade, P. A. R., Aghanim, N., et al. 2016, A&A, 594, A27
Planck Collaboration, Aghanim, N., Arnaud, M., et al. 2011, A&A, 536, A9
Planck Collaboration, Aghanim, N., Arnaud, M., et al. 2012, A&A, 543, A102
Postman, M., Coe, D., Benítez, N., et al. 2012, ApJS, 199, 25
Priewe, J., Williams, L. L. R., Liesenborgs, J., Coe, D., & Rodney, S. A. 2017,
    MNRAS, 465, 1030
Rasia, E., Borgani, S., Ettori, S., Mazzotta, P., & Meneghetti, M. 2013, ApJ,
    776, 39
Redlich, M., Waizmann, J.-C., & Bartelmann, M. 2014, A&A, 569, A34
Richard, J., Kneib, J.-P., Limousin, M., Edge, A., & Jullo, E. 2010, MNRAS,
    402, L44
Richard, J., Stark, D. P., Ellis, R. S., et al. 2008, ApJ, 685, 705
Salmon, B., Coe, D., Bradley, L., et al. 2017, arXiv:1710.08930
Salmon, B., Coe, D., Bradley, L., et al. 2018, arXiv:1801.03103
Sereno, M., Giocoli, C., Ettori, S., & Moscardini, L. 2015, MNRAS, 449, 2024
Sereno, M., & Paraficz, D. 2014, MNRAS, 437, 600
Sunyaev, R. A., & Zeldovich, Y. B. 1972, CoASP, 4, 173
Trenti, M., Stiavelli, M., Bouwens, R. J., et al. 2010, ApJL, 714, L202
Turner, E. L., Ostriker, J. P., & Gott, J. R., III 1984, ApJ, 284, 1
Umetsu, K., Medezinski, E., Nonino, M., et al. 2014, ApJ, 795, 163
von der Linden, A., Allen, M. T., Applegate, D. E., et al. 2014, MNRAS, 439, 2
Von Der Linden, A., Best, P. N., Kauffmann, G., & White, S. D. M. 2007,
    MNRAS, 379, 867
Wen, Z. L., Han, J. L., & Liu, F. S. 2012, ApJS, 199, 34
Williams, L. L. R., Sebesta, K., & Liesenborgs, J. 2017, arXiv:1711.05265
Wong, K. C., Zabludoff, A. I., Ammons, S. M., et al. 2013, ApJ, 769, 52
Wyithe, J. S. B., Yan, H., Windhorst, R. A., & Mao, S. 2011, Natur, 469, 181
Zheng, W., Postman, M., Zitrin, A., et al. 2012, Natur, 489, 406
Zitrin, A., Broadhurst, T., Rephaeli, Y., & Sadeh, S. 2009a, ApJL, 707, L102
Zitrin, A., Broadhurst, T., Umetsu, K., et al. 2009b, MNRAS, 396, 1985
Zitrin, A., Fabris, A., Merten, J., et al. 2015, ApJ, 801, 44
Zitrin, A., Seitz, S., Monna, A., et al. 2017, ApJL, 839, L11
Zitrin, A., Zheng, W., Broadhurst, T., et al. 2014, ApJL, 793, L12